Accepted Manuscript

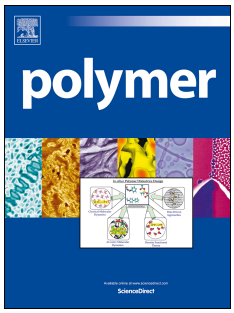

Molecular dynamics simulation of linear polyethylene blends: Effect of molar mass bimodality on topological characteristics and mechanical behavior

Ali Moyassari, Thomas Gkourmpis, Mikael S. Hedenqvist, Ulf W. Gedde

PII: S0032-3861(18)31117-0

DOI: https://doi.org/10.1016/j.polymer.2018.12.012

Reference: JPOL 21099

To appear in: *Polymer*

Received Date: 8 August 2018

Revised Date: 25 October 2018

Accepted Date: 6 December 2018

Please cite this article as: Moyassari A, Gkourmpis T, Hedenqvist MS, Gedde UW, Molecular dynamics simulation of linear polyethylene blends: Effect of molar mass bimodality on topological characteristics and mechanical behavior, *Polymer* (2019), doi: https://doi.org/10.1016/j.polymer.2018.12.012.

Submitted to Polymer

Molecular Dynamics Simulation of Linear Polyethylene Blends: Effect of Molar Mass Bimodality on Topological Characteristics and Mechanical Behavior

Ali Moyassari [a, *], Thomas Gkourmpis [b], Mikael S. Hedenqvist [a], Ulf W. Gedde [a, *]

[a] *Fibre and Polymer Technology, School of Engineering Sciences in Chemistry, Biotechnology and Health, KTH Royal Institute of Technology, SE-100 44 Stockholm, Sweden*

[b] *Innovation & Technology, Borealis AB, SE-444 86 Stenungsund, Sweden*

Abstract

Blending different molar mass fractions of polyethylene (PE) in order to obtain materials with higher fracture toughness has previously proven beneficial. Our approach has been to use coarse-grained (CG) molecular dynamics (MD) simulations to obtain semicrystalline polyethylene systems on a nanoscale, and then draw them in order to mimic tensile testing. The CG potentials were derived, validated and utilized to simulate melt equilibration, cooling, crystallization and mechanical deformation. Crystallinity, tie chain and entanglement concentrations were continuously monitored. During crystallization, the low molar mass fraction disentangled to a greater degree and ended up with a lower entanglement density than the high molar mass fraction, although the tie chain concentration was higher for the low molar mass fraction. The deformation behavior of semicrystalline PE above its glass transition temperature was then assessed in a uniaxial tensile deformation simulation. The low-strain mechanical properties (i.e. elastic modulus, yield stress and strain) were in accordance with the literature. The high-strain mechanical features and toughness were improved in bimodal systems. The presence of a high molar mass fraction in bimodal systems was shown to affect the crystallinity and tie chain concentration during the strain hardening, leading to tougher model systems. Finally, the bimodal system with equal shares of the molar mass fractions showed the highest toughness and the best ultimate mechanical properties while having a concentration of tie chains and entanglements intermediate between the values for the other systems. This was a clear sign of the non-exclusive role of tie chains and entanglements in the mechanical behavior of bimodal PE and more generally of semicrystalline polymers at high strains.

Keywords: semicrystalline polyethylene; coarse-grained molecular dynamics; tie chains and entanglements

1. Introduction

Polyethylene (PE) with a bimodal molar mass distribution is a high-performance material for applications such as blow-molded containers and flexible packaging films with a higher strength and lower weight than the traditional unimodal alternatives. The increased resistance to slow crack growth of bimodal PE also makes it the state-of-art material for water, gas and sewage pipes with long service life [1], [2].

The structure-property relationships of multimodal PE have been studied [3–8], and it is believed that the tie chains are responsible for the superior properties of bimodal PE, because they exist at a higher concentration in bimodal than in unimodal systems [3,9–11]. The primary structural parameter (PSP2) introduced by Rohlfing and DesLauriers [12] is believed to be correlated to the fracture toughness. In their work they coupled size exclusion chromatography (SEC) and infrared (IR) spectroscopy to obtain both molar mass and co-monomer distributions and subsequently used the Huang and Brown tie chain model [13] to calculate a PSP2 value, which has been used to justify and predict the mechanical performance of bimodal PE [4], [14].

The role of entanglements formed during crystallization and their impact on the fracture toughness of bimodal PE needs further study. A single chain can participate in several crystalline and amorphous regions, forming tie chains and entanglements, which are known to play a vital role in the mechanical performance of the material [15–17]. In bimodal PE, these topological features of a polymer chain may differ depending on its length and branch content.

Monte Carlo (MC) and molecular dynamics (MD) simulations have been used to assess crystallization [18–23], microstructure [18], [24–26], and the mechanical behavior of semicrystalline polymers [15], [25], [27–30], but these studies usually deal with model systems

with molecules having a single chain length or an ensemble of molecules with a unimodal molar mass distribution. Nevertheless, there are only few studies dealing with the simulation of crystallization of bimodal polymers. Triandafilidi et al. [31] used coarse-grained (CG) MD to study the crystallization of poly(vinyl alcohol) (PVA) with both unimodal and bimodal molar mass distributions. Luo et al. [32] studied the crystallization of long PVA chain mixtures with very short chains (ca. 5 repeating units), which were considered to be the solvent phase, and investigated the effect of chain topology on the crystallization behavior. Jiang et al. [33] assessed the growth rates of polymer co-crystallization in the binary mixtures of two chain lengths.

Our aim was to use MD simulation to study the molecular characteristics that affect the crystallization and the fracture toughness of bimodal PE. There are two main routes to model semicrystalline polymers at an atomistic level: (1) The polymer chains are arranged in layered structures with crystalline lamellae and amorphous layers and MC/MD is performed to equilibrate the structure [24], [27], [34], [35]; (2) A liquid polymer structure is equilibrated and thereafter crystallized into a semicrystalline structure [18], [22], [32], [36]. The first approach may result in realistic microstructures (lamellar stacks), whereas the second approach generates less-organized structures that may better resemble the natural equilibrium structures, especially with regard to deformation mechanisms during the drawing of the systems at high strains [22]. However, there is a difference between the microstructures obtained through the latter approach and experimental observations due to computationally inevitable higher cooling rates, which correspond to extreme quenching [22]. We used the second approach. First, we derived CG potentials using reference atomistic MD simulations on linear model PE systems and we then used the CG potentials obtained in MD simulations to equilibrate, cool and crystallize bimodal PE melts to obtain semicrystalline structures. When the desired equilibrated semicrystalline

models had been obtained, uniaxial tensile deformation MD simulations were performed on the systems. The topological features (tie chains, entanglements etc.) and thermodynamic properties were continuously monitored from the beginning (molten state) until fracture in the tensile deformation simulation.

The work was divided into two separate but related comparative studies: The study described in the present paper, which exclusively deals with linear bimodal PE systems, all the focus being on the bimodal character of the systems to assess its effects on tie chain and entanglement concentrations, crystallization and mechanical behavior of the material. A second paper [37], deals with more realistic bimodal PE model systems that have short-chain branches on the high molar mass fraction, as in industrially relevant materials [38], and compares the results with the results presented in the present paper. Short-chain branches act as defects for the crystallization [17], [39] and consequently alter the morphology of the semicrystalline state. For instance, thinner lamellae have been observed in short chain branched systems [17], [39], [40], and these affect the mechanical behavior of the material [17], [40]. Hence, distinguished studies for the effects of bimodality and short-chain branches are necessary, and these lead to in-depth investigations of each case.

2. Simulation models and methods

2.1. Model systems

Five systems were studied designated US100, B7525, B5050, B2575, and UL100 where U: unimodal, B: bimodal, S: a chain with 320 carbon atoms, L: a chain with 1280 carbon atoms, and the numbers denote the mass percentage of the S and L chains. Due to computational limits, the chosen model chains were shorter than the chains of the real bimodal materials, but the short

chains were sufficiently long to form entanglements [41] and the long chains were significantly longer than the short chains to mimic the bimodal character of 'practical' systems.

Table 1. Compositions of model PE systems

System	n_S[a]	n_L[a]
US100	1280	-
B7525	960	80
B5050	640	160
B2575	320	240
UL100	-	320

[a] n_S and n_L are the numbers of short and long chains, respectively.

The model systems were sufficiently large to provide statistically reliable results and avoid finite-size issues [27], and they were computationally affordable for the equilibration, cooling and tensile deformation simulations. Each system consisted of 409 600 carbon atoms. The cooling rate used was $0.2\,\mathrm{K\,ns^{-1}}$. The number of systems studied made it impossible to use united atom potentials to describe the atomistic interactions, but the coarse-grained method was found to be very efficient. This method allowed computationally fast equilibration and cooling simulations for larger systems and also made it possible to assess highly strained systems [22], [30], [31], [36], [42], [43].

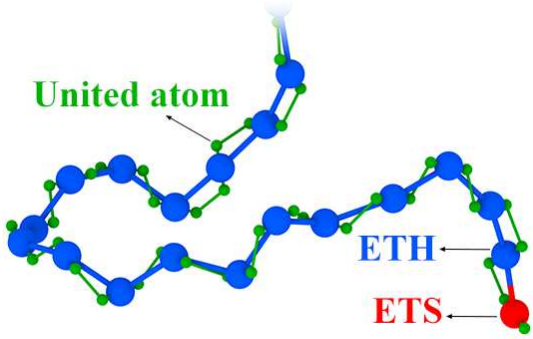

Fig. 1. Representation of the mapping scheme used in this study. The chain-end bead (ETS) and backbone beads (ETH) are illustrated with red and blue colors, respectively. The united atoms are shown in green. The molecular visualizations were made with the OVITO package [44].

2.2. Coarse-graining

Fig. 1 shows the coarse-grained mapping scheme used in this study. Each backbone PE repeating C_2H_4 unit and chain-end C_2H_5 unit were mapped as ETH and ETS beads with masses of 28.0532 and 29.0611 g mol^{-1}, respectively. The center of mass was maintained in the mapping procedure. A set of potentials capable of describing the coarse-grained linear PE system were derived using the iterative Boltzmann inversion (IBI) method included in the MagiC package [45]. Classical MD simulations were first performed on linear atomistic reference systems and simulation trajectory snapshots were stored. The mapping scheme, bonded and non-bonded interaction types were assigned to MagiC, whereafter the MagiC used the stored trajectory snapshots and the mapping scheme as input and calculated the reference radial distribution function (RDF) between bead pairs, using a 25 Å cutoff, as well as the bond length and angle distributions between consecutive backbone beads. In the IBI procedure which was then performed, MagiC started from direct inverse Boltzmann potentials calculated from collected distribution data after which, starting from a CG mapped structure, it sampled the potential phase

space through a certain number of MC steps in each iteration. At the end of each iteration, it calculated a new set of CG potentials based on the distribution data obtained for the simulated mapped system and applied corrections with the aim of reproducing the reference distribution data. The detailed IBI procedure can be found elsewhere [45]. It was typically performed for about 50 iterations each for a total of 2×10^7 equilibration and sampling steps, until the RDF deviation between MC sampled CG distributions and the reference distributions was less than 2 %.

2.3. Atomistic molecular dynamics simulations

Three separate atomistic amorphous systems consisting of 200 linear chains of $C_{100}H_{202}$ were generated at 450 K, using the EMC package [46], [47]. Molecular dynamics simulations with an initial equilibration at 450 K, cooling to a temperature of 350 or 300 K, and finally production runs were performed in the NPT ensemble, the target temperature and atmospheric pressure being fixed using the Nosé–Hoover thermostat [48] and Parrinello–Rahman barostat [49]. Periodic boundary conditions were applied. The TraPPE-UA (transferable potentials for phase equilibria, united atom version) force field was used to describe the atomistic potentials both for the melt generation step and for MD [50–52]. Previously, the TraPPE-UA has been shown to reproduce reasonably well a good number of important properties of both linear [23] and branched [34] PE systems in the melt [23] and semicrystalline state [35], [23]. The 14 Å cutoff was used for the van der Waals interactions. With a time step of 1 fs, Newton's equations of motion were integrated using a leap-frog algorithm [53]. Each atomistic MD simulation in the production runs resulted in a 400 ns trajectory of which the first 100 ns were considered only as equilibration. The atomistic MD simulations were carried out using the GROMACS 5.1.2 package [54].

2.4. Coarse-grained potentials

The best practice of CG potentials derived using the standard IBI is at the particular pressure and temperature of the reference atomistic system used. However, depending on the coarsening level, the potentials can remain valid to describe the system in a temperature range surrounding this particular thermodynamic point [55]. The coarser the mapping scheme, the smaller is the valid temperature range of application [56], [39]. Since the CG mapping scheme used was not very coarse, it is assumed that the valid temperature range covers ±50 K of the temperature of the reference atomistic system. The CG potentials were calculated separately at 300 K, 350 K and 450 K in order to be applied to systems including a temperature range from 300 to 450 K. The final CG potentials obtained using IBI describe the bond stretch, bond angle and non-bonded pair interactions between the PE beads.

2.5. Coarse-grained molecular dynamics simulations

For all five model systems, CG simulations were performed using the derived CG potentials: The systems were equilibrated at 450 K for 200 ns, cooled at a rate of $0.2\ \mathrm{K\,ns^{-1}}$ from 450 K to 400 K using the CG potentials for 450 K followed by cooling at the same rate from 400 K to 350 K using CG potentials for 350 K. Finally, the systems were equilibrated at 350 K for 100 ns using the CG potentials derived at 300 K. The latter potentials were used to make the crystal stems more distinct, i.e. straighter and less thermally distorted. After obtaining an equilibrated semicrystalline system, the uniaxial tensile deformation simulation was performed at 350 K on all systems, using a computationally affordable true strain rate of $5\times10^{7}\ \mathrm{s^{-1}}$. This combination of high strain rate and high temperature was expected to reproduce the mechanical behavior of the material being stretched at a lower strain rate and temperature thus closer to experimental conditions [28,57,58]. The draw direction was chosen as the direction with which the crystalline

CG bonds were least correlated, according to the section 2.7. During the deformation, atmospheric pressure was maintained in the other two directions. The LAMMPS package [59] was used for all the CG simulation runs. The Nosé-Hoover [48], [60] thermostat and barostat were used with damping parameters of 100 and 1000 time steps, respectively. Also, to speed up the simulations while taking care of energy conservation, especially for the fastest degrees of freedom (bond stretching and bending), a multiple time step algorithm, the reversible reference system propagator algorithm (rRESPA) integrator, was used. This algorithm decouples slow and fast degrees of freedom using different Liouville operators for each, making it possible to use more than one time step for integration of the different degrees of freedom [61]. Time steps of 1, 2 and 8 fs were used for the stretching, bending and non-bonded interactions, respectively. A cutoff of 16 Å was used for non-bonded interactions. The CG trajectory snapshots and thermodynamic properties of the systems were stored for analysis at 1 ns and 0.2 ps intervals during the formation stage, and at 0.5 ns and 0.2 ps intervals during the tensile deformation stage.

2.6. Entanglement analysis

The entanglement analysis methods that use pure geometrical criteria are quicker [62] and more proper [27] than other methods when inhomogeneous semicrystalline systems such as those in this study are to be considered. The fastest and most frequently used geometrical method is the Z1-code [62–65] used in this study. The Z1-code examines the primitive path network of a given trajectory snapshot and determines several interesting topological properties, of which we were mainly interested in Z, the number of entanglements (number of kinks) in each polymer chain, and N_e^{kink}, the number of CG beads between the entanglement points in each chain, which are related through the equation [64]

$$N_e^{kink}(N) = \frac{N(N-1)}{Z(N-1)+N} \quad (1)$$

where N is the number of CG beads per molecule. The Z1-code also calculates the number of CG beads between entanglement points, based on the end-to-end distance and contour length of the primitive path of a chain, but this latter approach is less appropriate for semicrystalline systems as the conformations of the chains are no longer Gaussian [18,32].

2.7. Tie chain and crystallinity analysis

An in-house MATLAB code was developed to quantify the polymer mass crystallinity X_C, the average crystal stem length $\bar{d}$, the tie chain concentration and average orientation parameter $\bar{S}$. This algorithm used three filters to recognize the crystal stems in each molecule:

1. For each CG bead i, the average angle θ_1 between bond $\vec{V}_{i,i+1}$ and 10 neighboring bonds was calculated. Based on the bond angle distribution calculated for the CG mapped reference atomistic system at 300 K (shown in Fig. 2a), the CG bond angle of $165° \leq \theta_1 \leq 180°$ could belong to a crystal stem.

2. The angle θ_2 between two consecutive vectors that connect every second bead (i.e. the angle between vectors of $\vec{V}_{i-2,i}$ and $\vec{V}_{i-1,i+1}$) should be less than 12°. The latter value is an arbitrary angle.

3. The angle θ_3 between two consecutive vectors that connect every third bead (i.e. the angle between vectors of $\vec{V}_{i-2,i+1}$ and $\vec{V}_{i-1,i+2}$) should be less than 12°.

The angles θ_1, θ_2 and θ_3 were acceptable within their defined ranges and not only as single values, in order to account for thermal distortion effects as well as the coarse nature of the CG system.

At least, 8 consecutive CG beads had to meet these three criteria to be accepted as a crystal stem. We are aware that this minimum crystal stem length of 8 beads (8 all-trans repeating units ~2 nm) is shorter than the established experimental minimum value of ~20 beads (5 nm) for an orthorhombic PE crystal [66], but crystalline regions, 8 beads thick or more, were actually formed in the modeled systems (Fig. S1). It was both observed in this study (see section "*3.3. Tie chains and crystallinity analysis in the formation stage*") and has also been reported elsewhere that the CG model of linear polymers results in a hexagonal crystal unit cell, which is different from the orthorhombic unit cell, but most important for this study was that the larger scale features of the crystals such as the lamellar structure and the folds along the chains were well reproduced [55]. A single trajectory snapshot was analyzed per time and the coordinates of all the crystal stem beads were stored. If the average angle θ_{Tie} between all the stem bond vectors of two consecutive crystal stems belonging to the same molecule was smaller than 165°, the chain segment connecting these stems was considered to be a tie. This $\theta_{Tie} < 165$ was visually examined thoroughly. The mass crystallinity X_C was calculated as the ratio of the number of CG bonds belonging to crystalline parts to the total number of bonds in the system. An average orientation parameter $\bar{S}$, similar to the Herman orientation parameter [67], was calculated for all crystalline CG bonds $\vec{V}$ with respect to the three main Cartesian unit vectors $\hat{\imath}$, $\hat{\jmath}$ and $\hat{k}$, parallel to the x, y and z axes, using:

$$\bar{S}_x = \frac{3\langle cos^2\theta_i \rangle - 1}{2}$$

$$\bar{S}_y = \frac{3\langle cos^2\theta_{\hat{j}}\rangle - 1}{2}$$

$$\bar{S}_z = \frac{3\langle cos^2\theta_{\hat{k}}\rangle - 1}{2} \quad (2)$$

where $\theta_{\hat{\imath}}$, $\theta_{\hat{j}}$ and $\theta_{\hat{k}}$ are the angles between an individual crystalline bond $\vec{V}$ and the respective unit vectors. For example, an average $\bar{S}_x = 1.0$ or $\bar{S}_x = -0.5$ means that all the CG crystal stem bonds are parallel or perpendicular to the x axis, whereas an average $\bar{S}_x = 0.0$ means that the average orientation of crystalline bonds with respect to the x axis is completely random. For tensile simulations, the model samples were stretched in the direction where the value of $\bar{S}$ was closest to 0 ($|\bar{S}| < 0.05$ was chosen for the draw direction for all samples).

3. Results and discussion

3.1. Coarse-grained potentials

Three non-bonded and four bonded CG potentials were derived for each of the three temperatures. The derived CG potentials reproduced the bond length, bond angle and non-bonded radial distribution of the mapped reference atomistic systems with a discrepancy of less than 2 %. Two examples are presented in Fig. 2. The same high convergence was observed between the other calculated atomistic and CG distributions (not shown here).

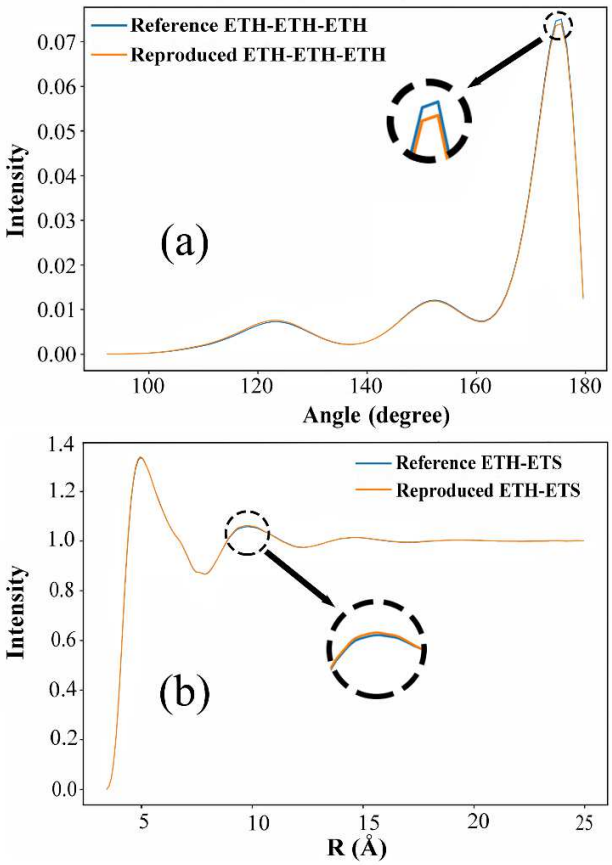

Fig. 2. Reproduction of the reference distribution data using the CG potentials for (a) the ETH-ETH-ETH bond angle distribution for the PE model obtained at 300 K, and (b) the ETH-ETS non-bonded radial distribution function for the PE model obtained at 450 K.

The isobaric thermal expansion coefficient α was calculated for the UL100 by cooling it from 410 K to 400 K and using the equation [23]:

$$\alpha = \frac{1}{V}\left(\frac{\delta V}{\delta T}\right)_p = \left(\frac{\delta[\ln V]}{\delta T}\right)_p \quad (3)$$

where V, T and p are the volume, temperature and pressure of the system, respectively. The $\alpha = 6.21 \times 10^{-4}$ K^{-1} obtained was comparable with the experimental data range ($6.96 - 7.38 \times 10^{-4}$ K^{-1}) [68] and the value of 7.2×10^{-4} K^{-1} for linear $C_{1000}H_{2002}$ at 400 K previously simulated using the TraPPE-UA force field [69].

The isothermal compressibility β was calculated for the UL100 using thermodynamic data for the final 70 ns of the equilibration run at 450 K, during which the density was stable, using the equation [69–71]:

$$\beta = \frac{1}{k_B T} \times \frac{\langle V^2 \rangle - \langle V \rangle^2}{\langle V \rangle} \quad (4)$$

where k_B is the Boltzmann constant. The $\beta = 1.45 \times 10^{-4}$ atm^{-1} obtained was comparable with the experimental value of 1.11×10^{-4} atm^{-1} at 440 K for HDPE [68].

The densities of the equilibrated UL100 and US100 melts were 0.787 g cm^{-3} and 0.783 g cm^{-3} in agreement with the simulated values of respectively 0.780 g cm^{-3} and 0.773 g cm^{-3} for linear $C_{1000}H_{2002}$ and $C_{320}H_{642}$ at 450 K obtained using the TraPPE-UA force field [69].

Using the Z1-code, the average numbers of entanglements per chain (Z) for US100 and UL100 equilibrated at 450 K were calculated to be 9.6 and 36.5, respectively. These larger values were comparable with the values of 8.4 and 30.0 obtained by simulations [69] using the TraPPE-UA force field. The average end-to-end distance $\langle {R_{ee}}^2 \rangle^{1/2}$ and contour length of the primitive path $\langle L_{PP} \rangle$ obtained were respectively 86.9 and 188.0 Å for the equilibrated US100. These values are larger than those obtained by atomistic simulations, 78.1 and 164.0 Å [69]. The inevitable less

detailed nature of the CG potentials is the reason for the discrepancy. For instance, no dihedral angle distribution was considered when deriving the CG potentials. The CG potentials were used in order to be able to simulate several, otherwise computationally expensive, model systems for long simulation run times and to compare their topologies and mechanical behavior. The observed errors in topological characteristics followed the same trend for both the short and the long chains e.g. higher entanglement concentration was observed for both US100 and UL100. Thus, the errors are assumed to be of minor importance for this comparative study.

3.2. Entanglement analysis in the formation stage

It has been shown that the entanglement characteristics in the molten state, even at temperatures much higher than the crystallization temperature, affect the final semicrystalline state [18], [72]. It is therefore helpful to follow the evolution of entanglement characteristics during the entire formation stage. Fig. 3a shows that the number of entanglements in US100 reached a plateau value by the end of the initial equilibration at 450 K. A higher long chain content required a longer equilibration time. Hence, if the equilibration time was longer than the currently used 200 ns, all the systems would have reached a similar entanglement concentration [69]. Fig. 3b, confirmed the Z results with more distinguished plateau values for the number of beads between entanglements . The first cooling took place over a period of 250 ns from $t = 200$ to $t = 450$ ns, during which time the model systems were cooled from 450 to 400 K using the CG potentials derived at 450 K. Fig. 3c shows a steady increase with time of the average end-to-end distance $\langle {R_{ee}}^2 \rangle^{1/2}$ which means that the chains became stiffer [69]. This is also observable in Fig. 3a, where the Z increased in agreement with other computational studies [18,72]. In the second cooling period from $t = 450$ to $t = 700$ ns, the systems were cooled from 400 to 350 K using the CG potentials derived at 350 K. In Figs 3a-d, at $t = 450$ ns, there is a

sudden vertical shift due to the change in CG potentials combined with the effect of restarting the MD run from the last checkpoint at $t = 450$ ns. This was an artifact of no physical significance. The chain stiffening continued until crystallization took place in the 360 – 365 K range. The sudden disentanglement shown in Fig. 3a and the increase in density in Fig. 3d were signs of crystallization [18,72]. There is a vertical density shift at 700 ns where the potential was switched to the potential derived at 300 K. This increase was because of the higher density of the atomistic reference system at 300 K than at 350 K. The systems shrank in size immediately after the potential switch, but rearrangement of polymer chains in order to alter the entanglement concentration requires longer times to occur. Thus, there was no shift in the entanglement concentration at 700 ns as correctly monitored by the Z1-code. During the crystallization the entanglements were less preserved for the short chains than the long chains, and the short chains thus had less entanglements in the semicrystalline state [17]. The concentrations of entanglements for each fraction (Fig. S2) also showed that, compared to the US100, the entanglement concentration of the short chain fraction in the final semicrystalline state was significantly higher with even as little as 25 wt.% long chains in the bimodal systems.

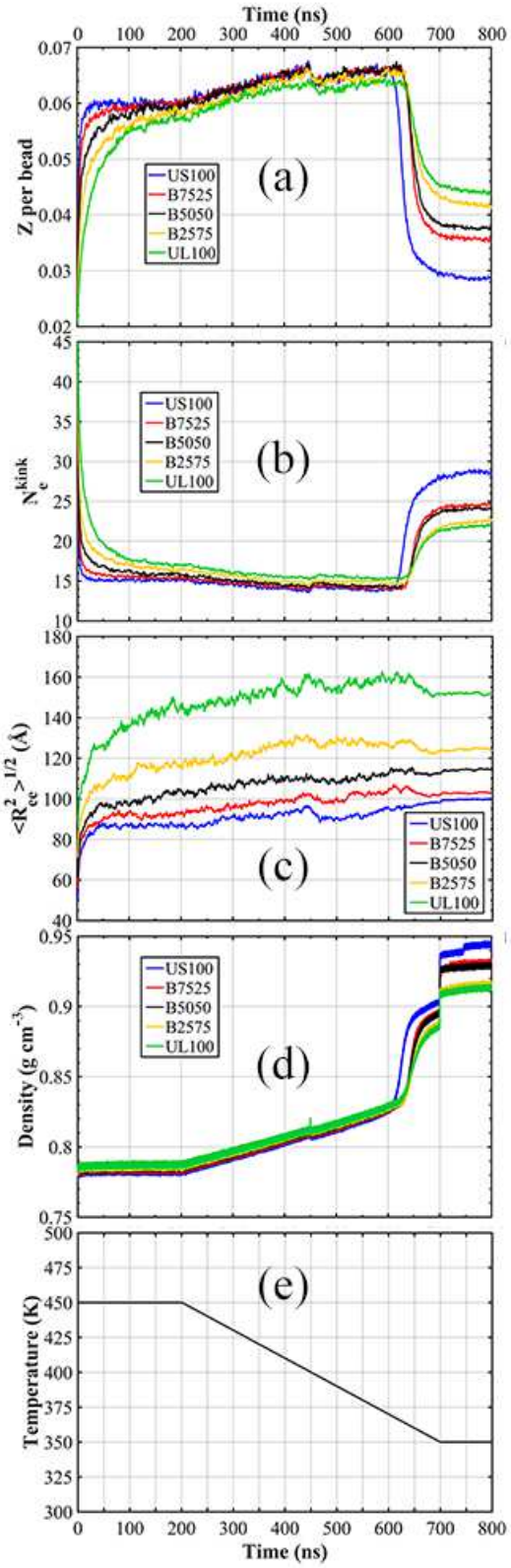
Time (ns)
Z per bead
US100
B7525
B5050
B2575
UL100
(a)
N_e^{kink}
(b)
$<R_{ee}^2>^{1/2}$ (Å)
(c)
Density (g cm^{-3})
(d)
Temperature (K)
(e)
Time (ns)

Fig. 3. Results of the entanglement analysis during the whole formation stage: (a) the average number of entanglements per CG bead, (b) the average number of beads between consecutive entanglements, (c) the average end-to-end distance $\langle {R_{ee}}^2 \rangle^{1/2}$, (d) the density, and (e) the temperature profile of the system during the formation stage included as a guide.

3.3. Tie chains and crystallinity analysis in the formation stage

Fig. 4 shows the results of tie chain concentration and crystallinity analysis. Figs 4a-c show that the onset temperature of crystallization decreased in the order US100, UL100, B5050, B7525 and B2575. It seems that a bidisperse chain length distribution, suppressed the crystallization onset temperature. This confirmed the result of an earlier theoretical study [73]. There was also a small secondary increase in density and crystallinity for US100 and B7525 during the final equilibration stage. It was more pronounced in US100 for which the average crystal stem length $\bar{d}$ also increased. Given that the short chains can translate faster than long ones, a local reorganization of the former could be responsible for this secondary increase in crystallinity. Again, the switch in potential to the one derived at 300 K was responsible for the vertical density shift at 700 ns. The mass crystallinity (density) of the systems was between 0.61 (0.943 g cm^{-3}) and 0.44 (0.915 g cm^{-3}), showing an increase with increasing low molar mass fraction. The X_C, density pair values obtained were in agreement with experimental data [12].

Switching the potentials at 700 ns increased the density of the system which corresponded to an increase in crystallinity as correctly tracked by the increase in the total number of crystalline bonds. However, the concentration of ties (Fig. 4d) dropped after the potential was switched. A careful visual inspection of the system trajectories before and after the potential switch (Figs S3 and S4) showed that the tie chain and crystallinity algorithm operated correctly and, as desired, the results after the potential switch were even more reliable. It should be noted that the tie chain

increase trend observed before the potential switch is correct, even though its absolute value is erroneous. The calculated results of tie chain and crystallinity algorithm before 700 ns should only be used to observe the general trends in the calculated properties such as increase in the average crystal stem length (Fig. 4(c)). The calculated values after the potential switch for the different model systems can be quantitatively compared. The final concentration of ties was higher in systems with a higher short chain fraction, which was less expected and was in contrast to the results for the number of entanglements (Fig. 3a). The relative difference in the final crystal thickness values at 800 ns (Fig. 4(c)) was less than 8 %, but the relative difference in the final crystallinity values was more significant. Considering the observed co-crystallization of both chain species and the similar average crystal stem lengths in all systems, it was expected to have higher tie chain concentration for systems with higher crystallinity as can be observed in Fig. 4(d).

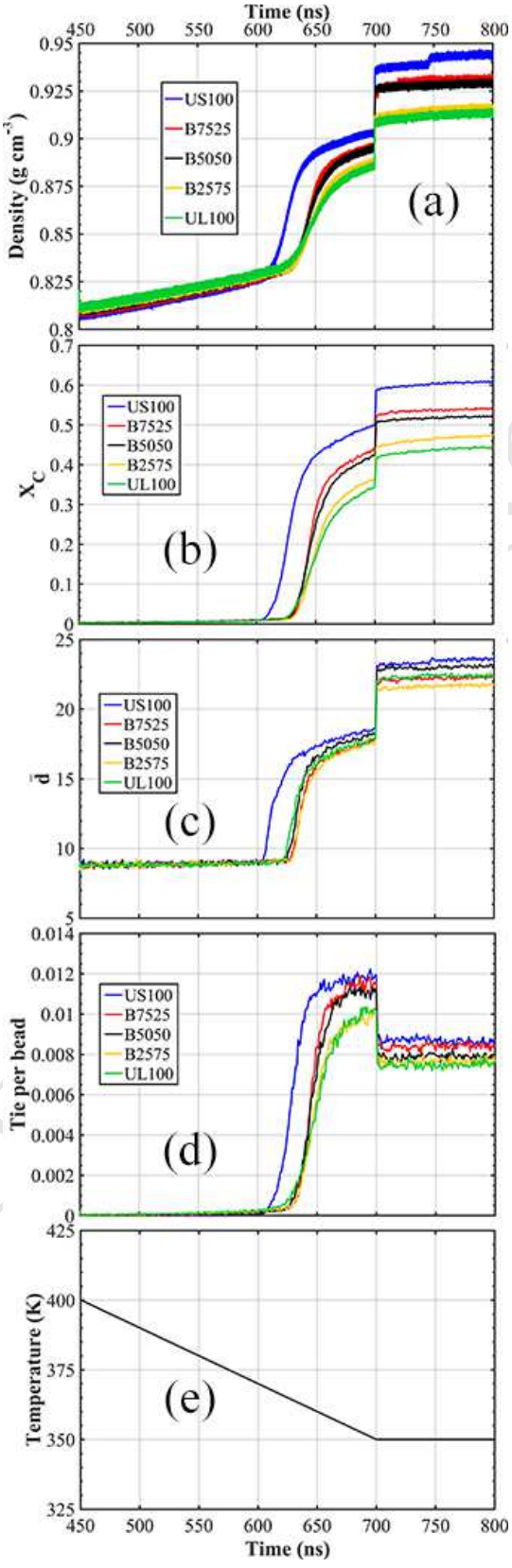
Time (ns)
Density (g cm^{-3})
US100
B7525
B5050
B2575
UL100
(a)
X_C
(b)
$\bar{d}$
(c)
Tie per bead
(d)
Temperature (K)
(e)
Time (ns)

Fig. 4. Results of crystallinity and tie chain analysis during the cooling and final equilibration stages: (a) the density, (b) the total mass crystallinity X_C, (c) the average number of beads in a crystal stem $\bar{d}$, (d) the average number of tie chains per bead, and (e) the temperature profile of the system included as a guide.

The thickening of the crystallites during the final equilibration phase was confirmed by the crystal stem length distribution just before the potential was switched (Fig. 5a) and at the end of equilibration stage at 350 K (Fig. 5b). The potential switch allowed the stems to grow longer, after which the average crystal stem $\bar{d}$ remained almost constant (Figs 4c, S5). It should be mentioned that, to further examine the tie chain and crystallinity determination algorithm, the final trajectory snapshot of UL100 was energy minimized using a conjugate gradient algorithm and the resulting structure was analyzed with regard to crystallinity. The crystallinity was 5 % higher in the energy minimized structure than in the structure prior to energy minimization. The content of tie chains showed a 10 % lower value in the energy-minimized structure than in the structure prior to energy minimization. This means that the equilibration method used efficiently accounted for the impact of thermal distortion.

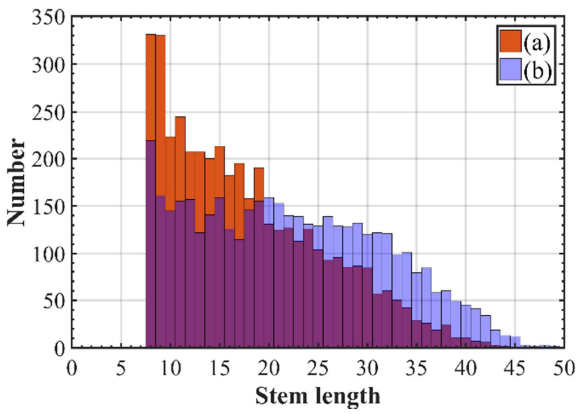

Fig. 5. A typical histogram showing the crystal stem length (beads) distribution of UL100 (a) just before the potential was switched at 700 ns, and (b) at the end of equilibration at 350 K at $t = 800$ ns.

Segregation of different molecular species during crystallization is observed in most polymers [67], and the blends of linear PE chains with different lengths are no exception. However, the degree of segregation depends on the difference in chain lengths of the components and on the cooling rate [74]. According to the lengths of the short and long chains the equilibrium melting points of both components were similar [67], thus, the cooling rate was more decisive. As a result of the high cooling rates and the fact that nucleation was homogeneous [18,75], only co-crystallization of the long and short chains was observed (Fig. 6). This computational limitation was good in that simulated co-crystallized systems resembled the real world bimodal PE materials with a very significant degree of co-crystallization of the low and high molar mass components, and this validated our chosen modelling approach to assess the mechanical behavior of bimodal PE. Fig. 7a confirmed the visual inspection of co-crystallization. Figs 7b and c show that the contribution of each fraction to total crystallinity and tie chain content was almost the same as their fractions present in the simulated systems.

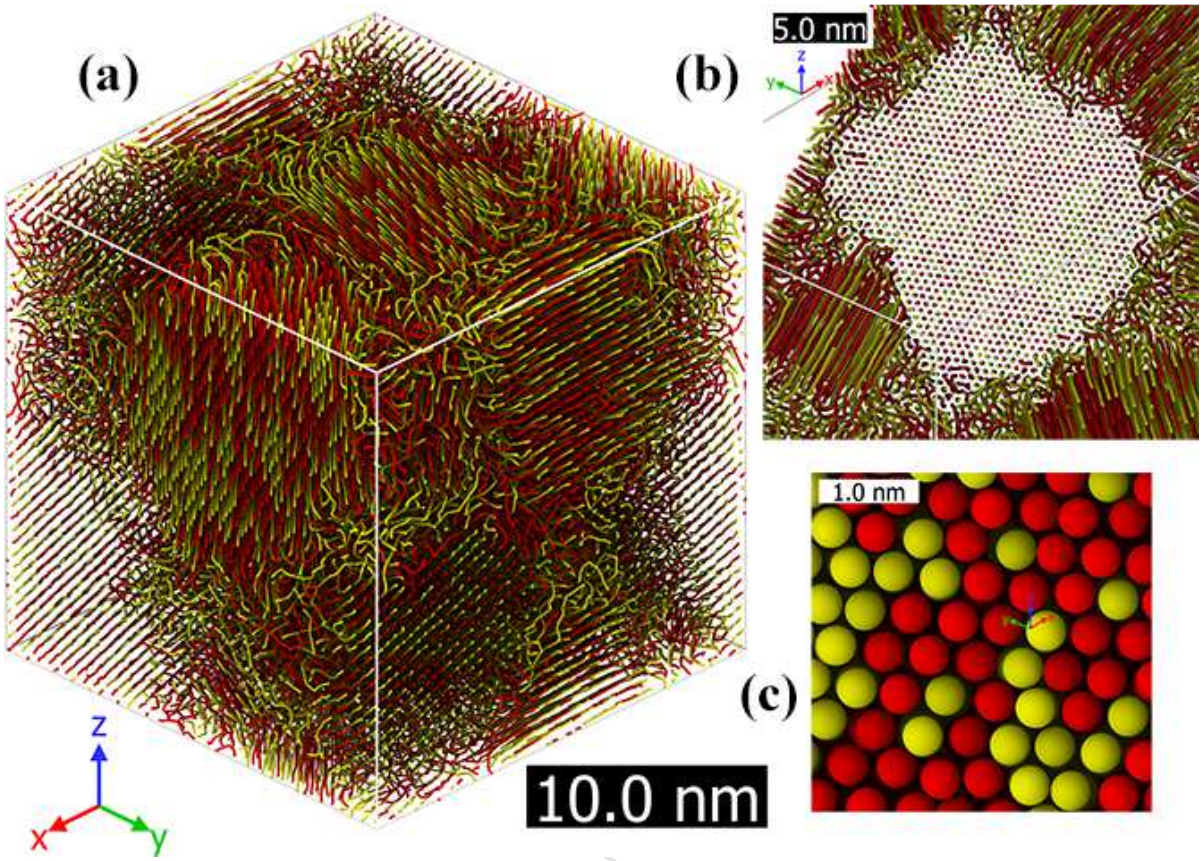

Fig. 6. The B5050 system at the end of the formation stage: (a) the semicrystalline structure with amorphous regions between crystalline parts, (b) a view normal to a 20 Å thick slice of the system, and (c) the hexagonal crystal unit cell type as well as the co-crystallization of short and long chains colored red and yellow respectively.

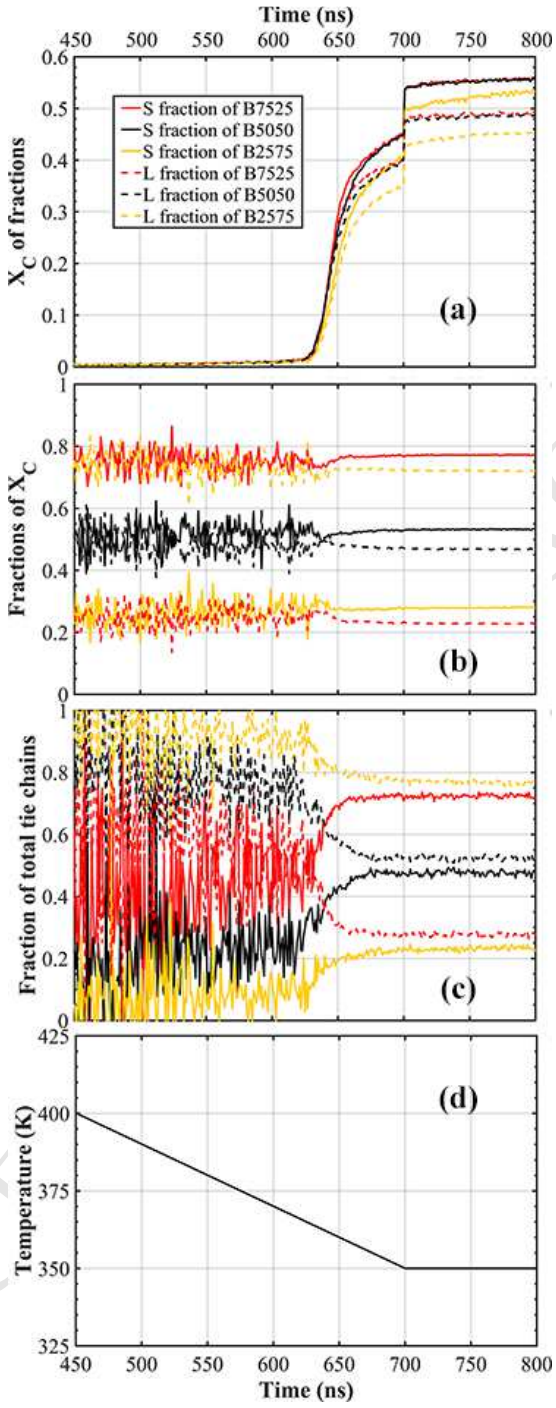

Fig. 7. The crystallinity and tie chain analysis for fractions of bimodal systems during the cooling and final equilibration stages: (a) the mass crystallinity X_C of fractions, (b) the contribution of each fraction to total mass crystallinity X_C, (c) the contribution of each fraction to

tie chains, and (d) the temperature profile of the system included as a guide. Note that the legend is the same for parts a, b and c.

3.4. Mechanical performance

The true stress-strain responses of the model systems are plotted in Fig. 8. The stress values obtained through the MD simulation fluctuated, so a moving average was applied in order to better visualize the behavior of the different samples. It was found in a recent study [76] that the stress oscillations occurring after the post-yield plateau are due to repeated chain melting and transport from crystalline to amorphous regions; these oscillations were very limited if explicit H-H and C-H repulsion interactions were used [76]. The oscillations were observed in the present study, but the main characteristics of the mechanical behavior of the model systems were reproduced sufficiently well to serve the purpose of comparison. Table 2 summarizes some selected mechanical properties of the systems. It is known that the elastic modulus of the non-oriented PE is a unique function of crystallinity [74,77]. This holds for the modulus results obtained except for UL100 with a modulus not very different from that of the bimodal systems B2575 and B5050. The modulus values were in agreement with simulation results of Yeh et al. [25] on samples stretched at the same strain rate and temperature. The yield stress is known to increase with increasing crystallinity [77], and the yield stress values showed the expected trend. The absolute values of stress and strain at the yield point were in good agreement with experimental data obtained at 20 °C for unimodal PE [77]. More interesting were the properties at failure i.e. at the maximum stress point. The stress-strain plots of the blends showed pronounced strain hardening than for US100. The B5050 was the toughest of all the modeled samples and showed the highest stress and strain at failure. This is, to our knowledge, the first time that the characteristic toughening effect of the mechanical behavior in bimodal PE blends

has been revealed using molecular simulation. The more realistic short-chain branched bimodal systems have been investigated in another study [37] (as mentioned in the introduction), which showed materials even tougher than their linear counterparts.

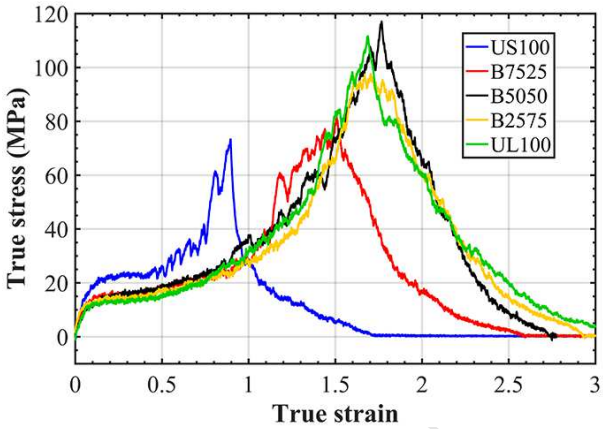

Fig. 8. The true stress-strain curves of the modeled systems.

Table 2. Mechanical properties of modeled PE systems

System	Elastic modulus[a] (MPa)	Yield[b] stress (MPa)	Yield[b] strain	Stress at failure[c] (MPa)	Strain at failure[c]	Toughness[d] (MPa)
US100	303	21.9	0.13	73.3	0.90	26
B7525	205	15.2	0.11	82.2	1.51	51
B5050	167	15.0	0.16	117.0	1.77	75
B2575	163	12.7	0.12	97.5	1.70	69
UL100	170	12.2	0.11	111.6	1.69	59

[a] Calculated from the true stress-strain data up to a strain of 0.05, according to ref. [36].

[b] The first peak stress (more easily observed in engineering stress-strain curves not shown here, then located accordingly) in the true stress-strain curves.

[c] The strain at the maximum stress value (failure point).

[d] Calculated by integration of the true stress-strain curve up to the failure point [77].

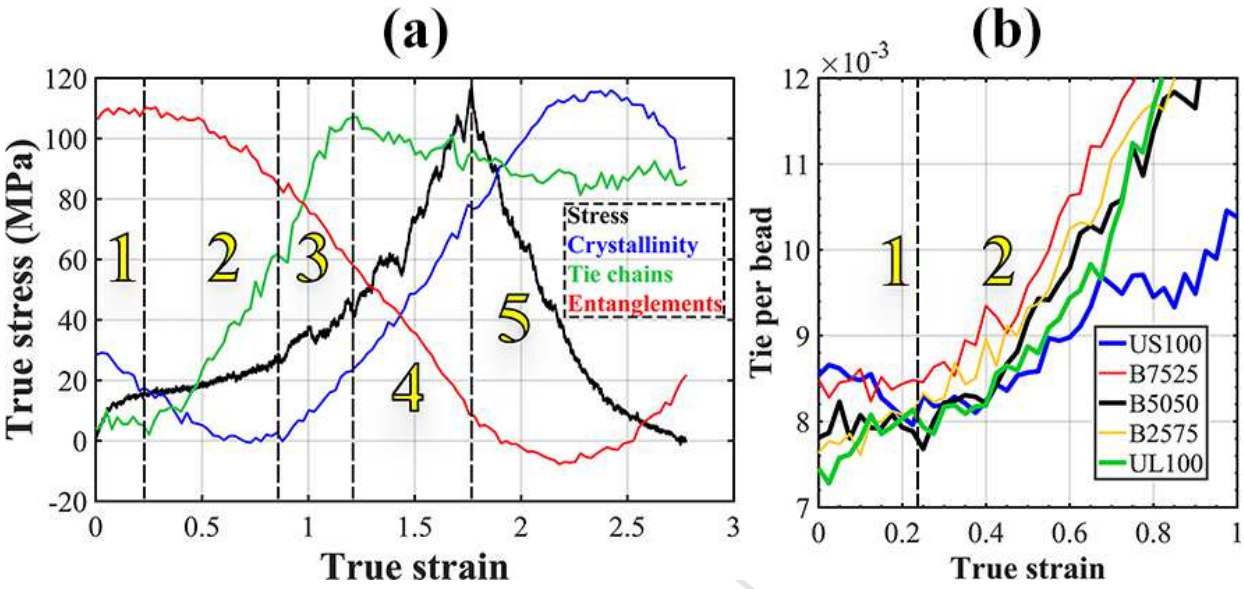

Fig. 9. (a) The crystallinity, tie chain and entanglement concentration superimposed on the stress-strain curve for the B5050 system. Note that the vertical axis presents only the stress values. (b) The zoomed tie chain per bead vs. strain for all the modeled systems.

3.5. Crystallinity and topological analysis in the deformation stage

Fig. 9a shows the crystallinity and the concentrations of tie chains and entanglements during deformation for B5050 as a representative bimodal system. The deformation process was divided into the following 5 stages: Stage 1 is from zero strain to a strain of ca. 0.1 above the yield point. In this region the number of entanglements remained constant (Figs 9a, 11) for all the systems, which was expected because the plastic deformation was small and the chain segments between entanglements were not fully stretched [77]. There was a small (ca. 5 %) decrease in mass crystallinity in stage 1 (Figs 9a, S6), due to (i) defects caused by force in the crystallites, with stems not parallel to the tensile direction (Fig. S7), in early small strains and (ii) lengthwise plane slides in crystallites [25,28,74,76–78] during and after the yield point. In the latter case, an

apparent increase in the number of tie chains could be expected since the previous loops entering the same crystal block were acting as tie chains connecting the slid blocks. However, other trends were also revealed: the number of tie chains decreased with increasing strain for US100, starting almost immediately on straining, whereas it showed an increase for UL100 (Fig. 9b). The disruption of small crystallites [78] (Fig. S8) was the reason for the reduction in the tie chains. These counteracting effects cancel out in B5050 and B7525, for which a plateau-like region was observed in the tie chain concentration curve. With a continuation of the deformation in stage 2, the post-yield plateau-like region was observed in the stress-strain curve; crystallites rotated towards the tensile direction (Fig. S9) and chain disentanglement was another apparent feature (Figs 9a, 11). The tie chain concentration showed an apparent increase, despite the decrease in crystallinity, due to the breakdown of some lengthwise-longer crystallites to smaller crystallites as indicated by the decrease in the average crystal stem length (Fig. S10), as well as by the decomposition (slippage) of wider crystallites to smaller narrower crystallites [78] (Fig. S11). There was a systematic overestimation of tie chains in the code as the result of disruptions along the crystal stems. However, most of the observed increase in the tie chain concentration was real. Plastic deformation continued in stage 3 where strain hardening occurred [77]. This was accompanied by an increase in crystallinity due to disentanglement and further alignment of the chains in the tensile direction (Fig. S12). The code might overestimate the increase in crystallinity but an overall increase in crystallinity was expected [79]. In stage 4, the strain hardening was very pronounced; the tie chain concentration leveled off, basically because almost all the crystalline bonds were aligned in the tensile direction leading to unification of some of the consecutive crystal stems, confirmed by the increase in the average crystal stem length (Fig. S10), which led to a reduction in the tie chain concentration. As shown in Fig. 10, the proportion

of long chains in the crystals and the tie chain concentration slightly increased during the later strain hardening region, which suggests that the long chains played a more important role in the strain hardening. The inability of US100 to recover its apparent initial crystallinity during the strain hardening is another sign of the lesser effect of short molecules in stabilizing the structure at higher strains. Comparing the entanglement densities at zero and failure strains in Fig. 11a shows that the bimodal systems tended to disentangle to a greater extent than the unimodal US100 system. This could explain their higher fracture toughness than that of US100. The similar decrease in entanglement shown in Fig. 11b for short and long chain fractions in the blends and in UL100 emphasized the effect of the incorporation of long chains in the blends and their dominating role for the entanglement density. Stage 5 started immediately after the failure point at which a void ca. 5nm in length had formed, and it continued until the stress became zero (fracture point). The void grew with increasing strain and formed a craze surrounded by highly elongated fibrilar strands of chains responsible for the increase in the crystallinity. The stress-relieved chains contracted to some extent and formed tilted crystallites (Fig. S13). As shown in Fig. 12, the volume of the system was preserved during deformation with less than 3 % increase until the end of stage 4 after which the voids formed and crazing occurred. Fig. 13 shows a 10 Å thick slice of the B5050 system at strains corresponding to the start and end trajectory snapshots of the different deformation regions, and makes it possible to observe the aforementioned morphological changes during the deformation.

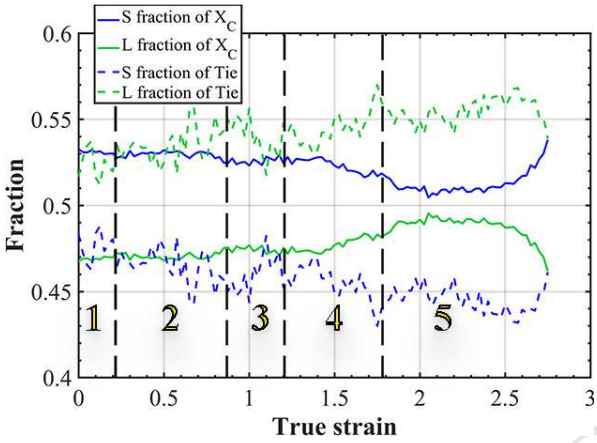

Fig. 10. The proportions of short and long chains in crystallinity and tie chain concentration plotted against the strain for the B5050 system. The deformation regions for the B5050 are also given.

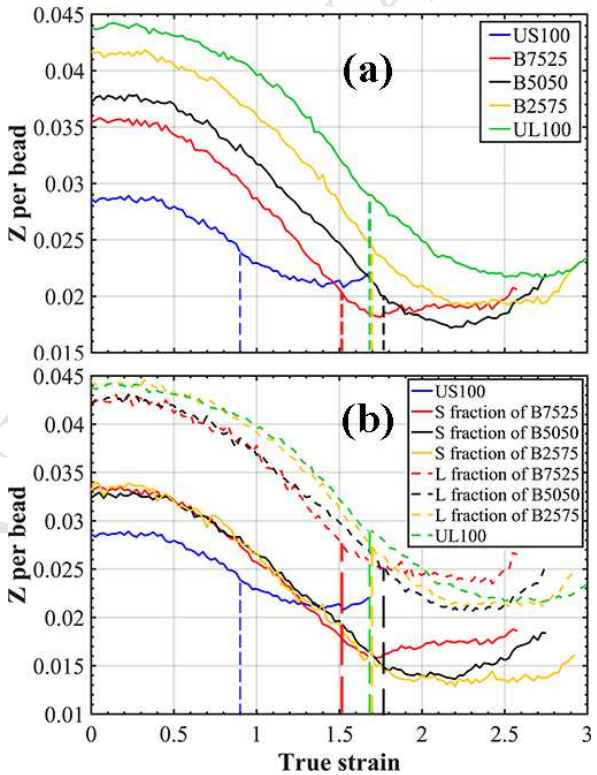

Fig. 11. (a) The average entanglement per bead vs. strain plotted from zero strain to the strain at which the stress again becomes zero. (b) The average entanglement per bead for each fraction. The failure strains are indicated by vertical broken lines for each system.

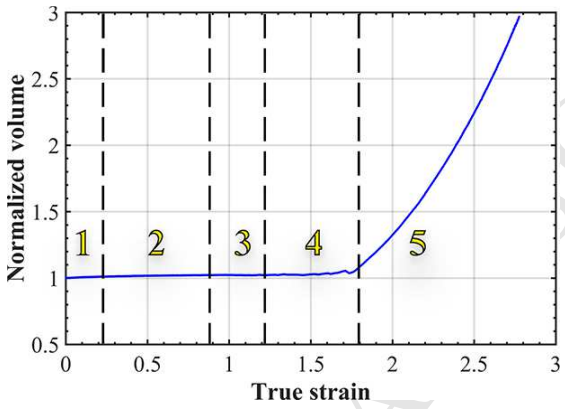

Fig. 12. The total volume of the system normalized with respect to the initial volume plotted against the strain for the B5050 system. The deformation stages for the B5050 are also given.

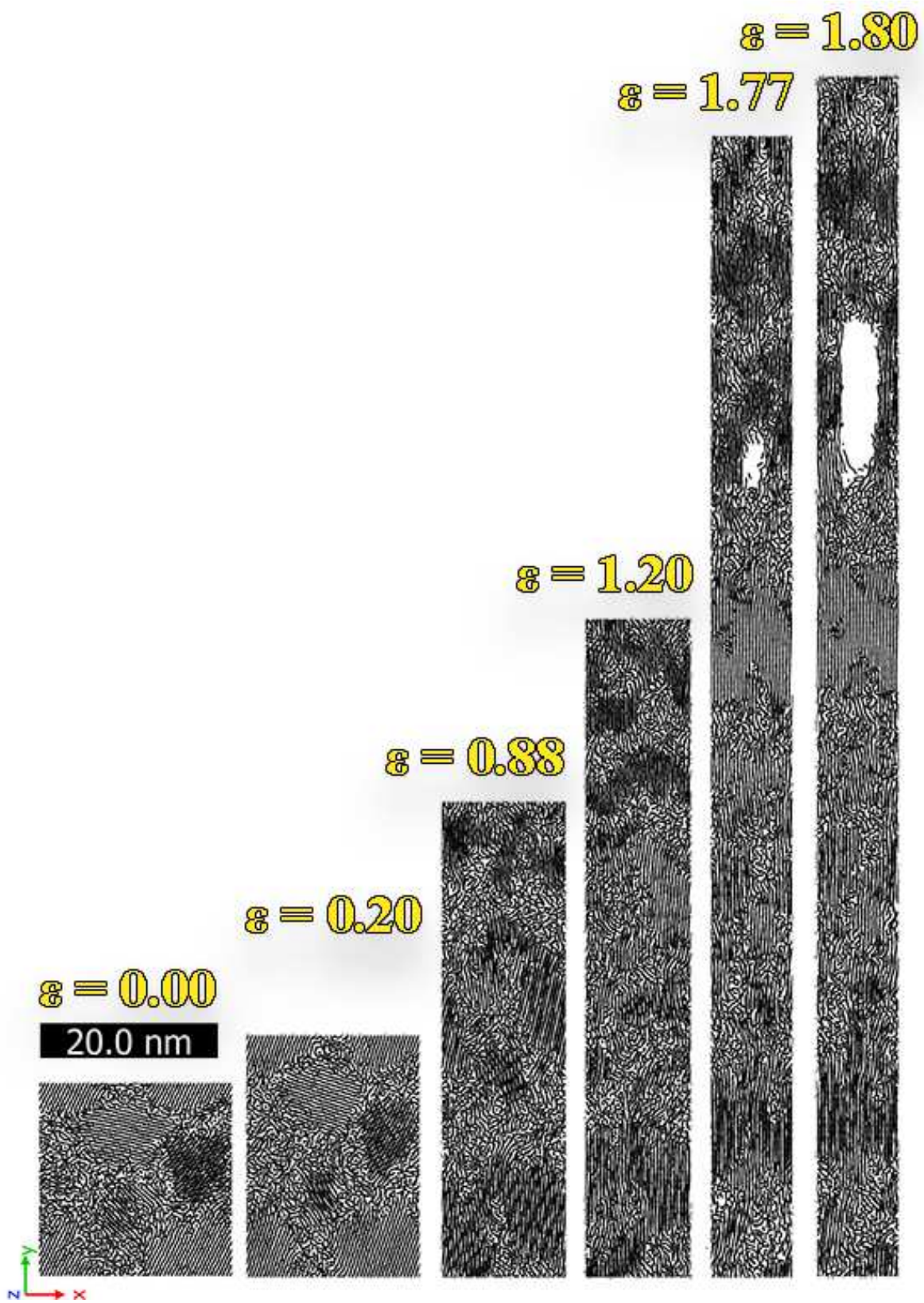
ε = 1.80
ε = 1.77
ε = 1.20
ε = 0.88
ε = 0.20
ε = 0.00
20.0 nm
Y
N
X

Fig. 13. The B5050 system shown in a view normal to a 10 Å thick slice of the system parallel to the xy plane. The strains at each trajectory snapshot correspond to the starting states of the deformation regions 1 to 5. The snapshot with strain $\varepsilon = 1.80$ is taken slightly after the beginning of region 5 and is presented to illustrate the craze development.

4. Conclusions

The effects of a bimodal molar mass distribution on tie chains and entanglements during crystallization and tensile deformation of linear semicrystalline PE systems were investigated using coarse-grained MD simulations. CG potentials were first derived based on atomistic reference trajectories at three temperatures using the IBI method, after which the CG potentials were used to simulate two unimodal and three bimodal linear systems of various compositions. The derived CG potentials successfully reproduced the bonded and non-bonded (RDF) distributions, with a discrepancy less than 2 %, as well as important thermodynamic properties (density, isobaric thermal expansion coefficient and isothermal compressibility). Furthermore, the derived CG potentials managed to reproduce topological features of the melt such as entanglement density, average end-to-end distance and contour length of the primitive path, and the results obtained were in good agreement with those reported for atomistic MD studies [69]. The potentials obtained were then used to equilibrate the model systems in the molten state at 450 K and subsequently cool them to 350 K initiating crystallization before final equilibration at 350 K prior to mechanical deformation simulations. Stiffening of the chains during cooling and their disentanglement during crystallization was observed. The systems crystallized through homogeneous nucleation as a consequence of rapid cooling rates necessitated by MD. This limitation helped the short and long chains to co-crystallize in proportion to their weight

percentages. Semicrystalline morphologies of randomly oriented crystallites were obtained. The structures showed characteristic features of melt crystallized PE on a nanometric scale, namely tie chains, entanglements, folded chains, loose loops and chain ends. An in-house code was developed to determine the mass crystallinity, crystal stem length distribution and tie chain concentration. These properties together with the entanglement density of modeled systems, were continuously monitored from the starting molten state to the mechanical fracture point. During the formation stage, average crystallinities, tie chain and entanglement concentrations of the bimodal systems were between the corresponding values for the unimodal systems. During the crystallization, the extent of disentanglement was greater for short chains than for long chains. At the end of the formation stage, a larger long chain fraction corresponded to a lower tie chain and a higher entanglement concentration. The incorporation of high molar mass fraction as low as 25 wt.% significantly increased the entanglement density of the system.

The uniaxial tensile deformation was performed on all model systems until failure, crazing and fracture were observed. The volume was successfully preserved until void formation and craze propagation occurred. The high-strain tensile properties were improved in the bimodal B5050 and B2575 systems which showed higher toughness values than unimodal systems. During the deformation, distinct strain regions were observed. The crystallinity decreased during the deformation until after the post-yield plateau at which strain hardening began and then increased until the fracture point. The entanglement concentration was almost constant up to slightly above the yield point, after which disentanglement was observed until the fracture point with higher rate of decrease in the strain hardening region (stages 3 and 4). The tie chain concentration showed different trends for short and long chain fractions at small strains. After the yield point, it increased until the middle of the strain hardening region, after which it started

to descend gradually until fracture occurred. The high molar mass fraction's share in crystallinity and tie chain concentration increased in the strain hardening region until the failure point. Finally, despite having intermediate concentrations of tie chains and entanglements, the B5050 sample proved to be the toughest system of all, which is contrary to the long believed "exclusive role" of tie chains or entanglements for improved toughness and ultimate mechanical properties of bimodal PE and of semicrystalline polymers in general.

Acknowledgment

The Swedish Research Council (Grant No. 621–2012–2673) and Borealis AB are acknowledged for the financial support. The MD simulations were performed on resources provided by the Swedish National Infrastructure for Computing (SNIC) at the Center for High Performance Computing (PDC, NSC and UPPMAX). Prof. Dr. Martin Kröger is acknowledged for kindly providing the Z1-code. Prof. A. Lyubartsev, Dr. A. Mirzoev and Dr. S. Mortezazadeh are acknowledged for their kind support regarding the MagiC package. Dr. Ir. Pieter in 't Veld is acknowledged for support for the EMC package. We thank Prof. Thomas Hjertberg and Dr. Yi Liu for fruitful discussions regarding the morphology and structure of multimodal PE.

Appendix A. Supplementary data

Supplementary data related to this article can be found here:

References

[1] M. Stürzel, S. Mihan, R. Mülhaupt, From Multisite Polymerization Catalysis to Sustainable Materials and All-Polyolefin Composites, Chem. Rev. 116 (2016) 1398–1433. doi:10.1021/acs.chemrev.5b00310.

[2] H. Knuuttila, A. Lehtinen, A. Nummila-Pakarinen, Advanced Polyethylene Technologies—Controlled Material Properties, in: A.C. Albertsson (Ed.), Long Term Prop. Polyolefins, Springer Berlin Heidelberg, Berlin, Heidelberg, 2004: pp. 13–28. doi:10.1007/b13519.
[3] L.L. Bohm, H.F. Enderle, M. Fleißner, High-density polyethylene pipe resins, Adv. Mater. 4 (1992) 234–238. doi:10.1002/adma.19920040317.
[4] R.A. García, A. Carrero, C. Martín, C. Domínguez, Effects of the structural components on slow crack growth process in polyethylene blends. Composition intervals prediction for pipe applications: Structural Components on Slow Crack Growth Process in PE blends, J. Appl. Polym. Sci. 121 (2011) 3269–3276. doi:10.1002/app.33911.
[5] M. Hedenqvist, M.T. Conde Braña, U.W. Gedde, J. Martinez-Salazar, Fracture of binary blends of linear and branched polyethylene, Polymer. 37 (1996) 5123–5129. doi:10.1016/0032-3861(96)00237-6.
[6] L. Hubert, L. David, R. Séguéla, G. Vigier, C. Degoulet, Y. Germain, Physical and mechanical properties of polyethylene for pipes in relation to molecular architecture. I. Microstructure and crystallisation kinetics, Polymer. 42 (2001) 8425–8434. doi:10.1016/S0032-3861(01)00351-2.
[7] X. Sun, H. Shen, B. Xie, W. Yang, M. Yang, Fracture behavior of bimodal polyethylene: Effect of molecular weight distribution characteristics, Polymer. 52 (2011) 564–570. doi:10.1016/j.polymer.2010.12.008.
[8] P.J. DesLauriers, N. Cole, M.C. Lamborn, C.G. White, B.K. Lavine, Chemometric Methods for Estimating the Strain Hardening Modulus in Polyethylene Resins, Appl. Spectrosc. 72 (2018) 463–475. doi:10.1177/0003702817745327.
[9] R. Seguela, Critical review of the molecular topology of semicrystalline polymers: The origin and assessment of intercrystalline tie molecules and chain entanglements, J. Polym. Sci. Part B Polym. Phys. 43 (2005) 1729–1748. doi:10.1002/polb.20414.
[10] J.J. Janimak, G.C. Stevens, Inter-relationships between tie-molecule concentrations, molecular characteristics and mechanical properties in metallocene catalysed medium density polyethylenes, J. Mater. Sci. 36 (2001) 1879–1884. doi:10.1023/A:1017517118154.
[11] Z. Zhou, N. Brown, B. Crist, Slow crack growth in blends of HDPE and model copolymers, J. Polym. Sci. Part B Polym. Phys. 33 (1995) 1047–1051. doi:10.1002/polb.1995.090330708.
[12] P.J. DesLauriers, D.C. Rohlfing, Estimating Slow Crack Growth Performance of Polyethylene Resins from Primary Structures such as Molecular Weight and Short Chain Branching, Macromol. Symp. 282 (2009) 136–149. doi:10.1002/masy.200950814.
[13] Y.-L. Huang, N. Brown, The effect of molecular weight on slow crack growth in linear polyethylene homopolymers, J. Mater. Sci. 23 (1988) 3648–3655. doi:10.1007/BF00540508.
[14] V. Voraruth, A. Caldera, J.B.P. Soares, S. Anantawaraskul, Polyolefins Made with Dual Metallocene Catalysts: How Microstructure Affects Polymer Properties, Macromol. Chem. Phys. (2018) 1700551. doi:10.1002/macp.201700551.
[15] Y. Men, J. Rieger, G. Strobl, Role of the Entangled Amorphous Network in Tensile Deformation of Semicrystalline Polymers, Phys. Rev. Lett. 91 (2003). doi:10.1103/PhysRevLett.91.095502.
[16] J. Cazenave, R. Seguela, B. Sixou, Y. Germain, Short-term mechanical and structural approaches for the evaluation of polyethylene stress crack resistance, Polymer. 47 (2006) 3904–3914. doi:10.1016/j.polymer.2006.03.094.

[17] S. Humbert, O. Lame, J.M. Chenal, C. Rochas, G. Vigier, New Insight on Initiation of Cavitation in Semicrystalline Polymers: In-Situ SAXS Measurements, Macromolecules. 43 (2010) 7212–7221. doi:10.1021/ma101042d.
[18] C. Luo, J.-U. Sommer, Frozen Topology: Entanglements Control Nucleation and Crystallization in Polymers, Phys. Rev. Lett. 112 (2014). doi:10.1103/PhysRevLett.112.195702.
[19] M.J. Ko, N. Waheed, M.S. Lavine, G.C. Rutledge, Characterization of polyethylene crystallization from an oriented melt by molecular dynamics simulation, J. Chem. Phys. 121 (2004) 2823. doi:10.1063/1.1768515.
[20] P. Yi, C.R. Locker, G.C. Rutledge, Molecular Dynamics Simulation of Homogeneous Crystal Nucleation in Polyethylene, Macromolecules. 46 (2013) 4723–4733. doi:10.1021/ma4004659.
[21] J.-U. Sommer, C. Luo, Molecular dynamics simulations of semicrystalline polymers: Crystallization, melting, and reorganization, J. Polym. Sci. Part B Polym. Phys. 48 (2010) 2222–2232. doi:10.1002/polb.22104.
[22] J. Morthomas, C. Fusco, Z. Zhai, O. Lame, M. Perez, Crystallization of finite-extensible nonlinear elastic Lennard-Jones coarse-grained polymers, Phys. Rev. E. 96 (2017). doi:10.1103/PhysRevE.96.052502.
[23] J. Ramos, J.F. Vega, J. Martínez-Salazar, Molecular Dynamics Simulations for the Description of Experimental Molecular Conformation, Melt Dynamics, and Phase Transitions in Polyethylene, Macromolecules. 48 (2015) 5016–5027. doi:10.1021/acs.macromol.5b00823.
[24] A. Moyassari, H. Mostafavi, T. Gkourmpis, M.S. Hedenqvist, U.W. Gedde, F. Nilsson, Simulation of semi-crystalline polyethylene: Effect of short-chain branching on tie chains and trapped entanglements, Polymer. 72 (2015) 177–184. doi:10.1016/j.polymer.2015.07.008.
[25] I.-C. Yeh, J.L. Lenhart, G.C. Rutledge, J.W. Andzelm, Molecular Dynamics Simulation of the Effects of Layer Thickness and Chain Tilt on Tensile Deformation Mechanisms of Semicrystalline Polyethylene, Macromolecules. 50 (2017) 1700–1712. doi:10.1021/acs.macromol.6b01748.
[26] S. Balijepalli, G.C. Rutledge, Conformational statistics of polymer chains in the interphase of semi-crystalline polymers, Comput. Theor. Polym. Sci. 10 (2000) 103–113. doi:10.1016/S1089-3156(99)00063-X.
[27] I.-C. Yeh, J.W. Andzelm, G.C. Rutledge, Mechanical and Structural Characterization of Semicrystalline Polyethylene under Tensile Deformation by Molecular Dynamics Simulations, Macromolecules. 48 (2015) 4228–4239. doi:10.1021/acs.macromol.5b00697.
[28] J.M. Kim, R. Locker, G.C. Rutledge, Plastic Deformation of Semicrystalline Polyethylene under Extension, Compression, and Shear Using Molecular Dynamics Simulation, Macromolecules. 47 (2014) 2515–2528. doi:10.1021/ma402297a.
[29] S. Jabbari-Farouji, J. Rottler, O. Lame, A. Makke, M. Perez, J.-L. Barrat, Correlation of structure and mechanical response in solid-like polymers, J. Phys. Condens. Matter. 27 (2015) 194131. doi:10.1088/0953-8984/27/19/194131.
[30] Y. Higuchi, M. Kubo, Deformation and Fracture Processes of a Lamellar Structure in Polyethylene at the Molecular Level by a Coarse-Grained Molecular Dynamics Simulation, Macromolecules. 50 (2017) 3690–3702. doi:10.1021/acs.macromol.6b02613.

[31] V. Triandafilidi, J. Rottler, S.G. Hatzikiriakos, Molecular dynamics simulations of monodisperse/bidisperse polymer melt crystallization, J. Polym. Sci. Part B Polym. Phys. 54 (2016) 2318–2326. doi:10.1002/polb.24142.
[32] C. Luo, M. Kröger, J.-U. Sommer, Entanglements and Crystallization of Concentrated Polymer Solutions: Molecular Dynamics Simulations, Macromolecules. 49 (2016) 9017–9025. doi:10.1021/acs.macromol.6b02124.
[33] X. Jiang, T. Li, W. Hu, Understanding the Growth Rates of Polymer Cocrystallization in the Binary Mixtures of Different Chain Lengths: Revisited, J. Phys. Chem. B. 119 (2015) 9975–9981. doi:10.1021/acs.jpcb.5b04108.
[34] V. Kumar, C.R. Locker, P.J. in 't Veld, G.C. Rutledge, Effect of Short Chain Branching on the Interlamellar Structure of Semicrystalline Polyethylene, Macromolecules. 50 (2017) 1206–1214. doi:10.1021/acs.macromol.6b02458.
[35] A. Moyassari, M. Unge, M.S. Hedenqvist, U.W. Gedde, F. Nilsson, First-principle simulations of electronic structure in semicrystalline polyethylene, J. Chem. Phys. 146 (2017) 204901. doi:10.1063/1.4983650.
[36] S. Jabbari-Farouji, O. Lame, M. Perez, J. Rottler, J.-L. Barrat, Role of the Intercrystalline Tie Chains Network in the Mechanical Response of Semicrystalline Polymers, Phys. Rev. Lett. 118 (2017). doi:10.1103/PhysRevLett.118.217802.
[37] A. Moyassari, T. Gkourmpis, M.S. Hedenqvist, U.W. Gedde, Molecular Dynamics Simulations of Short-Chain Branched Bimodal Polyethylene: Topological Characteristics and Mechanical Behavior, (Submitted for publication).
[38] P.J. DesLauriers, M.P. McDaniel, D.C. Rohlfing, R.K. Krishnaswamy, S.J. Secora, E.A. Benham, P.L. Maeger, A.R. Wolfe, A.M. Sukhadia, B.B. Beaulieu, A comparative study of multimodal vs. bimodal polyethylene pipe resins for PE-100 applications, Polym. Eng. Sci. 45 (2005) 1203–1213. doi:10.1002/pen.20390.
[39] J. Ramos, J.F. Vega, S. Sanmartín, J. Martínez-Salazar, Coarse-grained simulations on the crystallization, melting and annealing processes of short chain branched polyolefins, Eur. Polym. J. 85 (2016) 478–488. doi:10.1016/j.eurpolymj.2016.10.051.
[40] V. Stephenne, D. Daoust, G. Debras, M. Dupire, R. Legras, J. Michel, Influence of the molecular structure on slow crack growth resistance and impact fracture toughness in Cr-catalyzed ethylene-hexene copolymers for pipe applications, J. Appl. Polym. Sci. 82 (2001) 916–928. doi:10.1002/app.1923.
[41] M. Rubinstein, R.H. Colby, Polymer Physics, OUP Oxford, 2003. https://books.google.se/books?id=RHksknEQYsYC.
[42] B.L. Peters, K.M. Salerno, A. Agrawal, D. Perahia, G.S. Grest, Coarse-Grained Modeling of Polyethylene Melts: Effect on Dynamics, J. Chem. Theory Comput. 13 (2017) 2890–2896. doi:10.1021/acs.jctc.7b00241.
[43] A. Makke, O. Lame, M. Perez, J.-L. Barrat, Influence of Tie and Loop Molecules on the Mechanical Properties of Lamellar Block Copolymers, Macromolecules. 45 (2012) 8445–8452. doi:10.1021/ma301286y.
[44] Alexander Stukowski, Visualization and analysis of atomistic simulation data with OVITO–the Open Visualization Tool, Model. Simul. Mater. Sci. Eng. 18 (2010) 015012.
[45] A. Mirzoev, A.P. Lyubartsev, MagiC: Software Package for Multiscale Modeling, J. Chem. Theory Comput. 9 (2013) 1512–1520. doi:10.1021/ct301019v.

[46] P.J. in 't Veld, G.C. Rutledge, Temperature-Dependent Elasticity of a Semicrystalline Interphase Composed of Freely Rotating Chains, Macromolecules. 36 (2003) 7358–7365. doi:10.1021/ma0346658.
[47] P.J. In 't Veld, Enhanced Monte Carlo; http://montecarlo.sourceforge.net/emc/, (n.d.). http://montecarlo.sourceforge.net/emc/.
[48] W.G. Hoover, Canonical dynamics: Equilibrium phase-space distributions, Phys. Rev. A. 31 (1985) 1695–1697. doi:10.1103/PhysRevA.31.1695.
[49] M. Parrinello, A. Rahman, Polymorphic transitions in single crystals: A new molecular dynamics method, J. Appl. Phys. 52 (1981) 7182–7190. doi:10.1063/1.328693.
[50] K.A. Maerzke, J.I. Siepmann, Transferable Potentials for Phase Equilibria−Coarse-Grain Description for Linear Alkanes, J. Phys. Chem. B. 115 (2011) 3452–3465. doi:10.1021/jp1063935.
[51] M.G. Martin, J.I. Siepmann, Transferable Potentials for Phase Equilibria. 1. United-Atom Description of n-Alkanes, J. Phys. Chem. B. 102 (1998) 2569–2577. doi:10.1021/jp972543+.
[52] M.G. Martin, J.I. Siepmann, Novel Configurational-Bias Monte Carlo Method for Branched Molecules. Transferable Potentials for Phase Equilibria. 2. United-Atom Description of Branched Alkanes, J. Phys. Chem. B. 103 (1999) 4508–4517. doi:10.1021/jp984742e.
[53] R.W. Hockney, J.W. Eastwood, Computer Simulations Using Particles, McGraw-Hill, Oxford, 1981.
[54] M.J. Abraham, T. Murtola, R. Schulz, S. Páll, J.C. Smith, B. Hess, E. Lindahl, GROMACS: High performance molecular simulations through multi-level parallelism from laptops to supercomputers, SoftwareX. 1–2 (2015) 19–25. doi:10.1016/j.softx.2015.06.001.
[55] T. Vettorel, H. Meyer, Coarse Graining of Short Polythylene Chains for Studying Polymer Crystallization, J. Chem. Theory Comput. 2 (2006) 616–629. doi:10.1021/ct0503264.
[56] P. Carbone, H.A.K. Varzaneh, X. Chen, F. Müller-Plathe, Transferability of coarse-grained force fields: The polymer case, J. Chem. Phys. 128 (2008) 064904. doi:10.1063/1.2829409.
[57] E.N. Brown, R.B. Willms, G.T. Gray, P.J. Rae, C.M. Cady, K.S. Vecchio, J. Flowers, M.Y. Martinez, Influence of Molecular Conformation on the Constitutive Response of Polyethylene: A Comparison of HDPE, UHMWPE, and PEX, Exp. Mech. 47 (2007) 381–393. doi:10.1007/s11340-007-9045-9.
[58] J. Furmanski, C.M. Cady, E.N. Brown, Time–temperature equivalence and adiabatic heating at large strains in high density polyethylene and ultrahigh molecular weight polyethylene, Polymer. 54 (2013) 381–390. doi:10.1016/j.polymer.2012.11.010.
[59] S. Plimpton, Fast Parallel Algorithms for Short-Range Molecular Dynamics, J. Comput. Phys. 117 (1995) 1–19. doi:10.1006/jcph.1995.1039.
[60] W. Shinoda, M. Shiga, M. Mikami, Rapid estimation of elastic constants by molecular dynamics simulation under constant stress, Phys. Rev. B. 69 (2004) 134103.
[61] M. Tuckerman, B.J. Berne, G.J. Martyna, Reversible multiple time scale molecular dynamics, J. Chem. Phys. 97 (1992) 1990–2001. doi:10.1063/1.463137.
[62] S. Shanbhag, M. Kröger, Primitive Path Networks Generated by Annealing and Geometrical Methods: Insights into Differences, Macromolecules. 40 (2007) 2897–2903. doi:10.1021/ma062457k.
[63] M. Kröger, Shortest multiple disconnected path for the analysis of entanglements in two- and three-dimensional polymeric systems, Comput. Phys. Commun. (2005) 24.

[64] R.S. Hoy, K. Foteinopoulou, M. Kröger, Topological analysis of polymeric melts: Chain-length effects and fast-converging estimators for entanglement length, Phys. Rev. E. 80 (2009). doi:10.1103/PhysRevE.80.031803.
[65] N.C. Karayiannis, M. Kröger, Combined Molecular Algorithms for the Generation, Equilibration and Topological Analysis of Entangled Polymers: Methodology and Performance, Int. J. Mol. Sci. 10 (2009) 5054–5089. doi:10.3390/ijms10115054.
[66] L. Lin, A.S. Argon, Structure and plastic deformation of polyethylene, J. Mater. Sci. 29 (1994) 294–323. doi:10.1007/BF01162485.
[67] U.W. Gedde, Polymer Physics, Springer Netherlands, 1999.
[68] S.J. Han, D.J. Lohse, P.D. Condo, L.H. Sperling, Pressure-Volume-Temperature properties of polyolefin liquids and their melt miscibility, J. Polym. Sci. Part B Polym. Phys. 37 (1999) 2835–2844. doi:10.1002/(SICI)1099-0488(19991015)37:20<2835::AID-POLB3>3.0.CO;2-1.
[69] K. Foteinopoulou, N.C. Karayiannis, M. Laso, M. Kröger, Structure, Dimensions, and Entanglement Statistics of Long Linear Polyethylene Chains, J. Phys. Chem. B. 113 (2009) 442–455. doi:10.1021/jp808287s.
[70] M.P. Allen, D.J. Tildesley, Computer simulation of liquids, Clarendon Press, Oxford, 1987.
[71] N. Lempesis, P.J. in 't Veld, G.C. Rutledge, Atomistic Simulation of the Structure and Mechanics of a Semicrystalline Polyether, Macromolecules. 49 (2016) 5714–5726. doi:10.1021/acs.macromol.6b00555.
[72] C. Luo, J.-U. Sommer, Disentanglement of Linear Polymer Chains Toward Unentangled Crystals, ACS Macro Lett. 2 (2013) 31–34. doi:10.1021/mz300552x.
[73] J. Sommer, Kinetic phase diagram for crystallization of bimodal mixtures of oligomers as predicted by computer simulations, Polymer. 43 (2002) 929–935. doi:10.1016/S0032-3861(01)00656-5.
[74] R.K. Krishnaswamy, Q. Yang, Influence of phase segregation on the mechanical properties of binary blends of polyethylenes that differ considerably in molecular weight, Polymer. 48 (2007) 5348–5354. doi:10.1016/j.polymer.2007.07.018.
[75] S. Jabbari-Farouji, J. Rottler, O. Lame, A. Makke, M. Perez, J.-L. Barrat, Plastic Deformation Mechanisms of Semicrystalline and Amorphous Polymers, ACS Macro Lett. 4 (2015) 147–150. doi:10.1021/mz500754b.
[76] P.A.T. Olsson, P.J. in 't Veld, E. Andreasson, E. Bergvall, E.P. Jutemar, V. Petersson, G.C. Rutledge, M. Kroon, All-atomic and coarse-grained molecular dynamics investigation of deformation in semi-crystalline lamellar polyethylene, Polymer. (2018). doi:10.1016/j.polymer.2018.07.075.
[77] K. Jordens, The influence of molecular weight and thermal history on the thermal, rheological, and mechanical properties of metallocene-catalyzed linear polyethylenes, Polymer. 41 (2000) 7175–7192. doi:10.1016/S0032-3861(00)00073-2.
[78] G.R. Strobl, The physics of polymers: concepts for understanding their structures and behavior, 3rd. rev. and expanded ed, Springer-Verlag Berlin Heidelberg, New York, 2007.
[79] Z. Jiang, Y. Tang, J. Rieger, H.-F. Enderle, D. Lilge, S.V. Roth, R. Gehrke, W. Heckmann, Y. Men, Two Lamellar to Fibrillar Transitions in the Tensile Deformation of High-Density Polyethylene, Macromolecules. 43 (2010) 4727–4732. doi:10.1021/ma100303d.
[80] P. Mukherjee, A. Ghosh, N. Spegazzini, M.J. Lamborn, M.M. Monwar, P.J. DesLauriers, R. Bhargava, Relating Post-yield Mechanical Behavior in Polyethylenes to Spatially

Varying Molecular Deformation Using Infrared Spectroscopic Imaging: Homopolymers, Macromolecules. (2018). doi:10.1021/acs.macromol.8b00363.

Molecular Dynamics Simulation of Linear Polyethylene Blends: Effect of Molar Mass Bimodality on Topological Characteristics and Mechanical Behavior

Ali Moyassari [a, *], Thomas Gkourmpis [b], Mikael S. Hedenqvist [a], Ulf W. Gedde [a, *]

[a] *Fibre and Polymer Technology, School of Engineering Sciences in Chemistry, Biotechnology and Health, KTH Royal Institute of Technology, SE-100 44 Stockholm, Sweden*

[b] *Innovation & Technology, Borealis AB, SE-444 86 Stenungsund, Sweden*

Graphical abstract

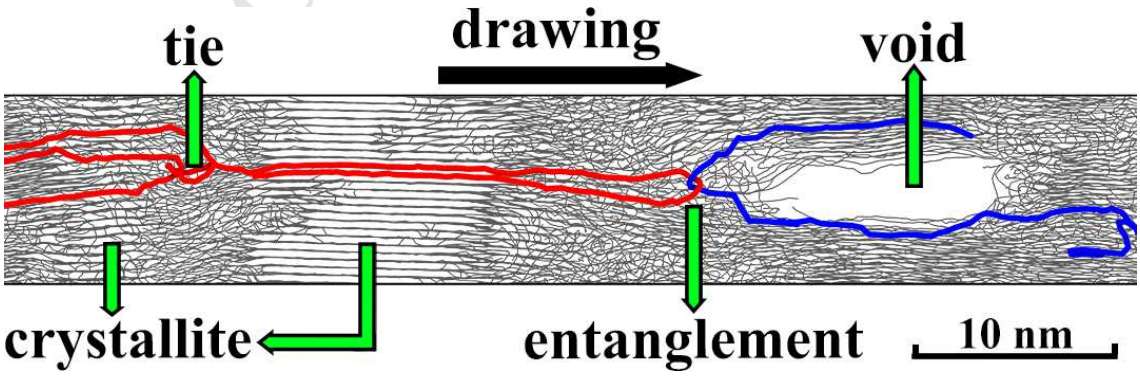

Highlights:

- Accurate coarse-grained potentials were derived to describe the interactions in linear PE.
- Unimodal and bimodal PE model systems were generated and crystallized using coarse-grained molecular dynamics.
- Crystallinity, tie chain and entanglement concentrations were continuously monitored during crystallization and tensile deformation simulations.
- Higher fracture toughness of bimodal PE systems was computationally revealed.